

Chapter 4

Simulation

4.1 Overview

This measurement used a detailed **GEANT3** simulation[90] of the particles and detector response. Simulation events started with the generation of muon(s) and beam line positron(s) at the end of the M13 channel, with rates that matched the DAQ scalers. Pions, protons, cloud muons and radioactive beam line particles were not simulated, since they were removed from the data by physical windows and a time of flight cut (see Section 3.3.1). The simulated particles and their secondaries³² were transported through the detector materials. When a muon decayed, the simulation produced a positron with energy and angle read from a separate database, which used a hidden value of $P_{\mu}^{\pi} \xi$ (see Sections 3.1 and 3.4). Transportation of the particles through the magnetic field used a fourth order Runge-Kutta numerical method. The muon's spin was transported with equivalent precision. The simulation demanded that at least one transportation step was taken in every material; this was important for the energy loss in thin materials such as the cathode foils.

The physics processes in the simulation included ionisation energy loss, δ -electron production, Bremsstrahlung, multiple Coulomb scattering, position annihilation, Compton scattering, pair production, and the photo-electric effect; these processes were *not* tuned from their **GEANT** defaults. Multiple scattering was particularly important for the muons since it affected the initial divergence of the beam, and the size of the beam measured by the wire chambers. The simulation included materials external to the tracking volume, such as the iron yoke, photomultiplier tube housing and scintillators; the positrons can backscatter from these materials and re-enter the tracking volume.

The simulation included a special digitisation routine, so that its output mimicked the real DAQ. This allowed the data and simulation to undergo an almost identical analysis; the exceptions were the crosstalk removal routine (see Section 3.2.2) and the time of flight cuts.

For each data set accumulated, a simulation with equivalent statistics was generated; this was adequate since the $P_{\mu}^{\pi} \xi$ precision is limited by systematic uncertainties, not statistical

³²These included γ 's, e^+ and e^- .

uncertainties.

The bespoke code modules that are important for $P_\mu^\pi \xi$ will be described. Specifically these are the particle generation routine, muon depolarisation mechanisms, muon decay generator, and the simulation of the chamber response. The simulation's performance is then documented.

4.2 Particle generation

The muon beam was measured before the solenoidal fringe field, using a pair of time expansion chambers (TECs); Appendix G described the analysis that resulted in the position (x, y) and angle (θ_x, θ_y) for each muon. The TECs had low positron efficiency, so that the beam line positrons were instead measured using the upstream drift chambers, while the magnetic field was off. The precision was inferior to the muon beam measurement, but was adequate since the muon decay parameters were relatively insensitive to the simulated positron beam.

For both the muons and beam line positrons, five x - y histograms were constructed with binning 0.1 cm, and these were filled with the number of particles, average θ_x , RMS (root mean square) of θ_x , average θ_y and RMS of θ_y . The initial particle position was chosen using an accept/reject method on the histogram of the number of particles. The θ_x and θ_y angles were then drawn from a Gaussian distribution with the mean and RMS from the other four histograms. The RMS was multiplied by a correction factor for multiple scattering, $c_x = 63.9\%$ in the x -module and $c_y = 48.0\%$ in the y -module. This approach fully accounted for correlations between position and angle, but assumed that θ_x and θ_y could be modelled by independent Gaussian distributions.

The muons were launched from a z -position corresponding to the centre of the TEC modules. The initial momentum (p) was found to linearly depend on the x -position at the TECs according to

$$p(x) = p_0 - p_1 x. \quad (4.1)$$

The p_1 parameter was tuned using comparisons such as Fig. 4.1, and $p_1 = 0.17$ MeV/c per cm was found to be optimal. The p_0 parameter was then determined by setting the average momentum to 29.6 MeV/c (see Section 2.2.4) so that

$$\begin{aligned} p_0 &= \langle p(x) \rangle + p_1 \cdot \langle x \rangle \\ &= 29.6 \text{ MeV/c} + (0.17 \text{ MeV/c}) \cdot \langle x \rangle, \end{aligned} \quad (4.2)$$

and $\langle x \rangle$ was different for each data set. Muons were not generated above the kinematic

maximum momentum of 29.79 MeV/c.

Section 2.9 described the materials traversed by the muons; the simulation required an extra 1.9 mg/cm² of material to match the data distribution of where the muon was last seen. However, this was within the uncertainties of the thickness measurements and the vacuum window bulge. For half of the simulations, the extra material was added to simulation, at a z location within the strong magnetic field region. For the other simulations there was no additional material.

4.3 Depolarisation

The simulation of the muon's spin will be described, by implementing Eq. (1.39) while in motion, and simulating time dependent depolarisation when the muon is stationary.

The simulation did not include depolarisation due to the field between the nucleus and atomic electrons, muonium formation at low velocities, and muon-electron scattering; see Section 1.6.2 for an explanation of why these were negligible. Also the spin of the positron is not transported since the experiment cannot detect this quantity.

4.3.1 Initial polarisation

The simulation starts muons with anti-parallel spin and momentum vectors. This is an approximation with two limitations; first the muons are selected from the graphite production target at an average depth of 16 μm . Multiple scattering while exiting the target changes the momentum vector but not the spin vector, causing them to no longer be anti-parallel. This effect is treated as a correction in Section 6.3.1. Second, the muons have already passed through the magnetic fields in the M13 beam line, and the difference in precession frequencies between the momentum and spin vectors (Eq. (1.37)) can change the angle between them. This second effect is negligible, changing P_μ at the level $\sim 10^{-8}$; see Appendix I for details of the estimate.

4.3.2 Electromagnetic field

Recall the Thomas equation from Section 1.6.1, which described the propagation of the spin vector in an electromagnetic field,

$$\frac{d\vec{s}}{dt} = \frac{e}{mc} \vec{s} \times \left[\left(\frac{g}{2} - 1 + \frac{1}{\gamma} \right) \vec{B} - \left(\frac{g}{2} - 1 \right) \frac{\gamma}{\gamma + 1} (\vec{\beta} \cdot \vec{B}) \vec{\beta} - \left(\frac{g}{2} - \frac{\gamma}{\gamma + 1} \right) \vec{\beta} \times \vec{E} \right]. \quad (1.39)'$$

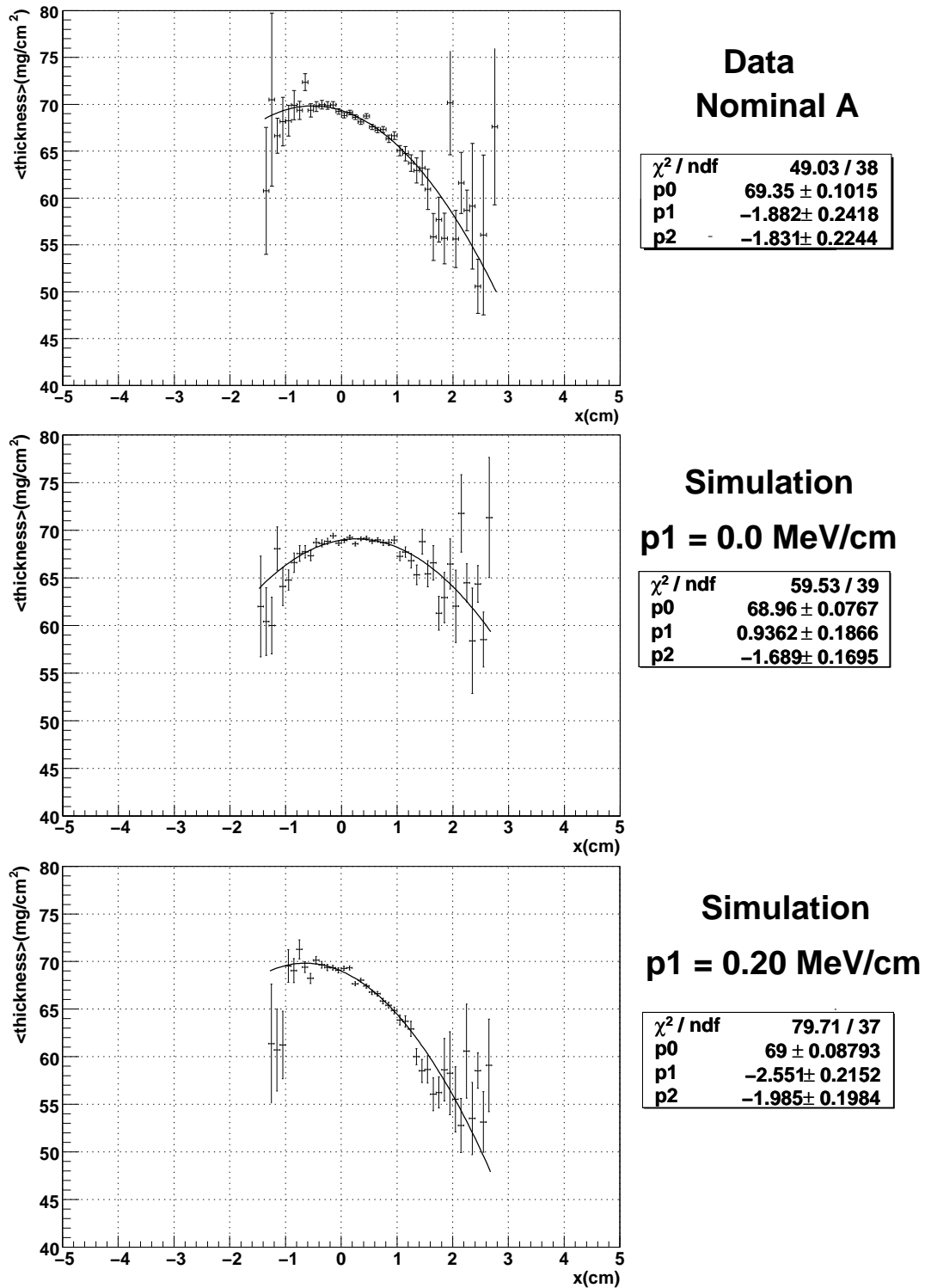


Figure 4.1: Average muon range (mg/cm^2) depends on the x -position of the muon at the TECs. The relationship is well modelled by a quadratic. The simulation required $p_1 = 0.17 \text{ MeV}/\text{cm}$ in order to match the data.

The E field term was not included in the simulation. The drift and proportional chambers have significant electric fields, but a field of $(+E)$ between the entrance cathode foil and wire was followed by a symmetric $(-E)$ field between the wire and exit cathode foil, cancelling the change in spin from this term. For programming convenience, the Thomas equation was manipulated into this form:

$$\frac{d\vec{s}}{dx} = \frac{d\vec{s}}{dt} \frac{1}{|\beta|} = \frac{e}{mc} \left[U_1(\vec{s} \times \vec{B}) - U_2(\vec{s} \times \vec{v}) \right], \quad (4.3)$$

where

$$U_1 = \left[\frac{1}{|\beta|} \left(a + \frac{1}{\gamma} \right) \right], U_2 = \left[a \frac{\gamma}{\gamma + 1} |\beta| (\vec{v} \cdot \vec{B}) \right],$$

and $a = (g - 2)/2$. The spin was then propagated using a Taylor expansion,

$$\vec{s} = \vec{s}' + \frac{d\vec{s}}{dx} \Delta x, \quad (4.4)$$

where \vec{s} is the new spin vector and \vec{s}' is the spin at the previous step. In order to correct for numerical precision errors, the components of the spin vector were renormalised at each step. For example,

$$s_z = \frac{s_z}{\sqrt{s_x^2 + s_y^2 + s_z^2}}, \quad (4.5)$$

and similarly for s_x and s_y . For each **GEANT** particle transportation step, smaller sub-steps were taken that depended on the magnitude of the magnetic field and muon velocity.

The Thomas equation can be solved exactly in a uniform and stationary magnetic field[94], and this solution was used to validate the numerical method[56]. A more recent test found that P_μ (the polarisation z -component) decreased by 4×10^{-4} within the tracking volume of the detector, where the field is ≈ 2.0 T and uniform, so that P_μ should be unchanged. This was due to not enough sub-steps being taken at low velocities to propagate s_x and s_y , which caused a s_z error due to the renormalisation in Eq. (4.5). This was fixed by increasing the number of sub-steps by a factor of ten. A new validation used the simulation with energy loss and multiple scattering disabled, to show that momentum and spin remained anti-parallel to $< 2 \times 10^{-5}$.

Note that **GEANT3** does not transport the spin by default, and the implementation in this section was unique to the TWIST experiment. **GEANT4** *does* include spin transportation by default, using the same fourth order Runge-Kutta algorithm as the momentum transportation code. This was insufficient motivation for moving to **GEANT4**, since the current Taylor expansion algorithm was valid for a $P_\mu^\pi \xi$ measurement at the level of 10^{-4} .

4.3.3 Time-dependent depolarisation

In the time interval between thermalisation and decay, the muon's spin is precessed, and can be flipped ($\vec{s} \rightarrow -\vec{s}$) so that $P_\mu(t)$ matches the data. The simulation does not implement the random walk of the muon in the metal stopping target (see Section 1.6.3).

4.4 Muon decay

The default GEANT3 program could simulate muon decays assuming the standard model ($V - A$) interaction ($P_\mu^\pi \xi = 1$). For non-standard model values of the decay parameters, a bespoke program was used[84], which included the higher order radiative corrections that were described in Section 1.4.5. The software ran on a dedicated server at TRIUMF, and each time a simulation began, the list of decay positron ($p, \cos\theta$) pairs was retrieved from the server.

The bespoke program also produced the derivative spectra that were described in Section 3.4. In this mode of operation, a ($p, \cos\theta$) pair *and* the relevant sign (\pm) were supplied to the simulation.

4.5 Wire chamber response

The responses of the DCs and PCs were simulated in detail, with the aim of accurately reproducing inefficiencies, bias and resolution. As a particle passed through the chamber gas, ion clusters were randomly produced along the trajectory, with a mean cluster spacing that was tuned to match the data. The drift distance to the wire was converted into a time using STRs from the GARFIELD software[92] (see Section 3.2.7). The time was then smeared to include electronics effects and diffusion. Wires that were dead in the data were removed from the simulation.

The muons produced more ionisation than the positrons, which deadened the wire within 0.06 cm, with a mean recovery time of $3.0 \mu\text{s}$. This effect is included in the simulation since it caused a small upstream inefficiency.

4.6 Performance

4.6.1 Upstream stops

Special “upstream stops data” were accumulated, where the muons were stopped close to the trigger scintillator, allowing the decay positrons to be reconstructed separately in each half of the detector. These data and the accompanying simulation provided guidance for the systematic uncertainties due to positron interactions and the upstream-downstream inefficiency.

At the time of writing, the upstreams stops analysis has been carried out for the nominal silver target, and a special larger radius aluminium target[95]. Two previous analyses have been made for the standard aluminium target[17, 56]. The larger target data were acquired with the target PCs removed, which increased the range of energies and angles reconstructed. This target differed from the standard aluminium, since it was lower purity (99% instead of > 99.999%), and was slightly thicker ($76 \mu\text{m}$ instead of $(71 \pm 1) \mu\text{m}$).

Positron interactions

The energy loss and angle changes between the upstream and downstream trajectories were compared in data and simulation. There will be discrepancies if the simulation has the incorrect target thickness, limitations in the positron interactions physics, a different resolution to the data, or a different reconstruction bias to the data.

The distribution of $(\Delta p) \cos \theta$ for the large aluminium target is shown in Fig. 4.2(a). The multiplication by $\cos \theta$ removes the dependence of energy loss on track length through the planar target module. $(\Delta p) \cos \theta > 0$ corresponds to an energy loss; the entries with $(\Delta p) \cos \theta < 0$ are due to the resolution of the reconstruction algorithm. The peaks of the data and simulation distributions differ by just $(1.2 \pm 0.1) \text{ keV}/c$ for the large aluminium target, with the simulation having slightly more energy loss than the data. This result is compared with the nominal targets in Table 4.1, where the simulation is seen to have about 6% more energy loss for all three targets. The FWHM of the distributions are well matched, and the latest preliminary results show an improvement in the data-simulation match from 10% down to about 3%. The remaining discrepancies in peak and FWHM could be due to an incorrect target thickness in the simulation, or a limitation in the modelling of positron energy loss. Note that the energy calibration procedure (Section 3.5) corrects for data-simulation differences in energy loss while positrons exit the target.

The systematic uncertainty due to the reproduction of hard scatters ($> 1.0 \text{ MeV}/c$) is constrained by the tail of Fig. 4.2(a). The most recent large target analysis finds that in the data (simulation), the fraction of events with $\Delta p > 1.0 \text{ MeV}/c$ is $1.054 \pm 0.008\%$

($1.069 \pm 0.009\%$), which is an agreement at the 1.9σ level; previously these numbers were $1.42 \pm 0.01\%$ ($1.420 \pm 0.004\%$)[17].

The change in angle through the target is well matched in data and simulation, as Fig. 4.2(b) demonstrates, with the peak positions differing by just (0.19 ± 0.02) mr for the large aluminium target. The peaks are matched at the sub-mrad level for the other targets (see Table 4.1). The cause of the non-zero peak angle is unknown and was not investigated, since a misalignment or bias of order 0.1 mr has negligible consequences for $P_\mu^\pi \xi$.

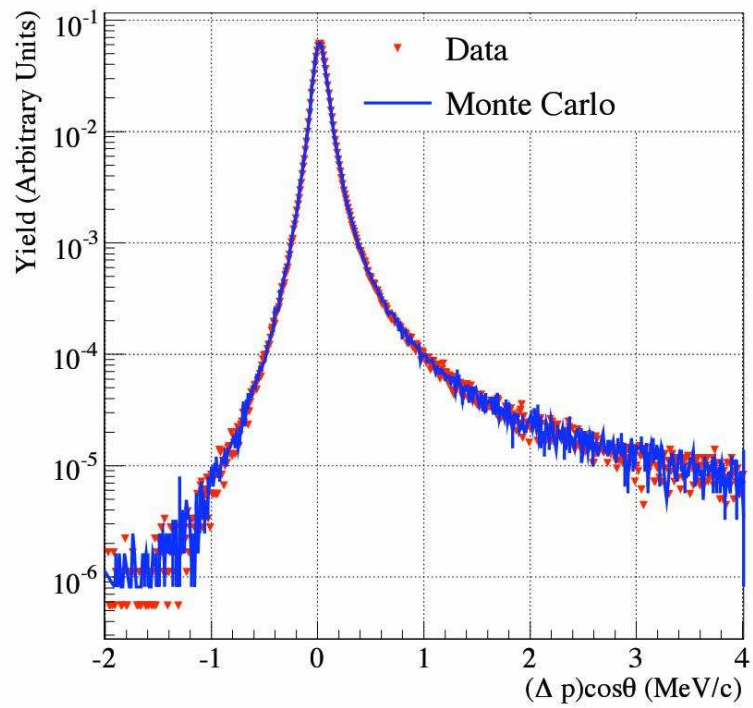
Table 4.1: Comparison of energy loss and scattering angle distributions in data and simulation. The latest results are preliminary. The bracketed number indicates the uncertainty on the final digit.

Target	Peak of $(\Delta p) \cos \theta$ (keV/c)		
	Data	Simulation	Difference
Nominal silver	41.7 (1)	44.2 (1)	-2.5 (1)
Nominal aluminium	32.8 (2)	-	-
Nominal aluminium[17]	28.4 (1)	29.65 (4)	-1.3 (1)
Large aluminium	21.0 (1)	22.2 (1)	-1.2 (1)

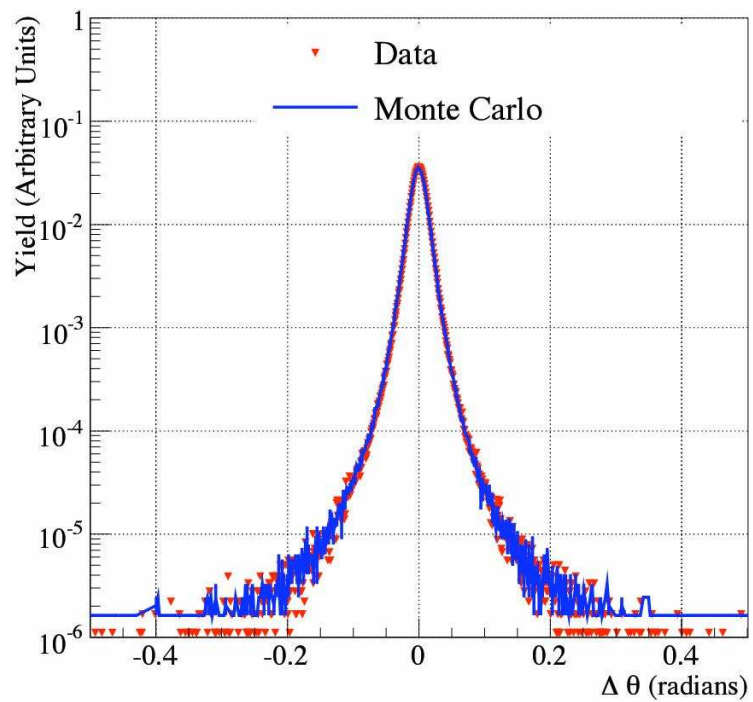
Target	FWHM of $(\Delta p) \cos \theta$ (keV/c)		
	Data	Simulation	Difference
Nominal silver	140.16 (8)	135.11 (6)	5.1 (1)
Nominal aluminium	130.50 (10)	-	-
Nominal aluminium[17]	155.90 (10)	141.64 (4)	14.3 (1)
Large aluminium	124.92 (7)	121.19 (8)	3.7 (1)

Target	Peak of $\Delta \theta$ (mr)		
	Data	Simulation	Difference
Nominal silver	-0.07 (4)	-0.21 (3)	0.14 (5)
Nominal aluminium	0.09 (4)	-	-
Nominal aluminium[17]	0.97 (2)	0.581 (7)	0.39 (2)
Large aluminium	0.11 (1)	-0.08 (2)	0.19 (2)

Target	FWHM of $\Delta \theta$ (mr)		
	Data	Simulation	Difference
Nominal silver	54.34 (3)	51.31 (2)	3.03 (4)
Nominal aluminium	28.58 (3)	-	-
Nominal aluminium[17]	29.75 (2)	29.159 (7)	0.59 (2)
Large aluminium	23.47 (1)	24.12 (1)	-0.65 (1)



(a) Energy loss.



(b) Angle change.

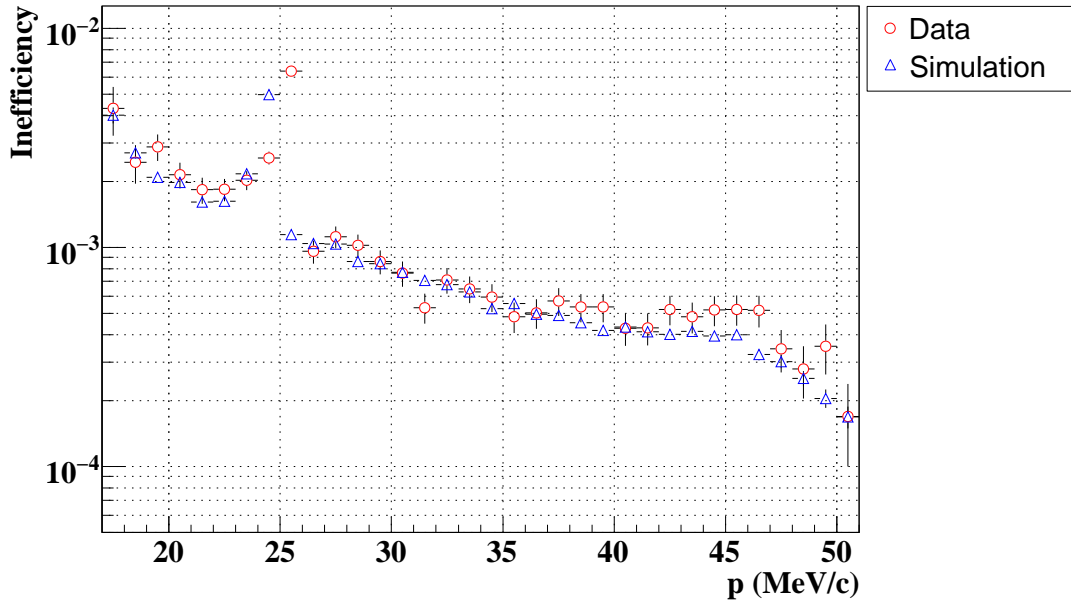
Figure 4.2: Energy loss and angle change for positrons traversing the large aluminium target[96].

Inefficiency

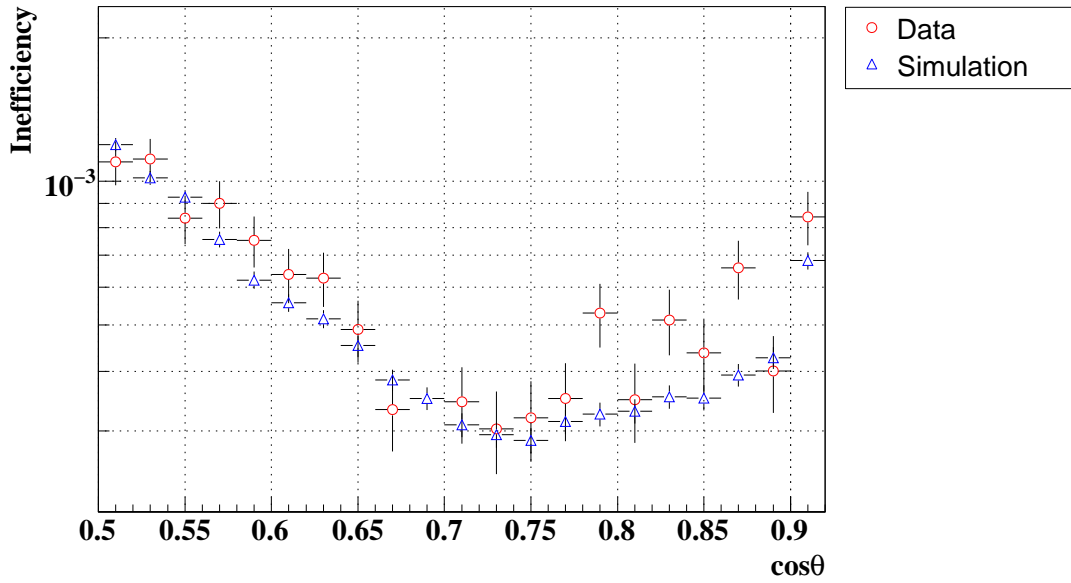
The chamber efficiencies were close to 99.95%, but the track reconstruction efficiency was lower due to ambiguity from particles overlapping and large angle scatters. The efficiency could be determined directly in simulation where the particle type and its trajectory were known, and was found to be $> 99.6\%$. An indirect track reconstruction inefficiency (TRI) measure was determined for both data and simulation, by using the upstream stops analysis to see how often a positron was reconstructed in one half of the detector, but not in the other; this measure cannot distinguish between decay positrons and beam positrons. The TRI is shown in Fig. 4.3, where a dependence on p and $\cos \theta$ is evident. The feature at $p = 25 \text{ MeV}/c$ corresponds to beam positrons, which were reconstructed with lower efficiency since they had small transverse momentum. The behaviour is well matched in data and simulation, except around the beam positron feature. If a cut is made at $(25 < p < 28) \text{ MeV}/c$, then to first order the difference between inefficiency in data and simulation is uniform over $(p, \cos \theta)$, and the average values of this difference are summarised in Table 4.2.

Table 4.2: Indirect track reconstruction inefficiency, determined by reconstruction of a positron in one half of the detector, but not the other half. In each case the average inefficiency is shown. The latest results are preliminary.

Target	Upstream inefficiency		
	Data	Simulation	Difference
Nominal silver			
Nominal aluminium			
Nominal aluminium[17]			
Large aluminium			
Target	Downstream inefficiency		
	Data	Simulation	Difference
Nominal silver			
Nominal aluminium			
Nominal aluminium[17]			
Large aluminium			



(a) Inefficiency for momentum slices.



(b) Inefficiency for angle slices.

Figure 4.3: Upstream track reconstruction inefficiency for the kinematic fiducial, determined by how often a positron is reconstructed in the downstream half of the detector, but not the upstream half[17].

4.6.2 Momentum resolution

The muon decay spectrum falls off steeply close to the kinematic endpoint (see Fig. 1.3). Since this feature is effectively a step function, its reconstructed width was used to compare the momentum resolution between data and simulation. The previous analysis found values of $\sigma(p) = 70 \text{ keV}/c$ for data and $\sigma(p) = 75 \text{ keV}/c$ for simulation, with uncertainties of less than $1 \text{ keV}/c$ [17]. For this analysis, the data and simulation both had a momentum resolution of $\sigma(p) = 60 \text{ keV}/c$; the better (*i.e.* smaller) resolution and the exact match between data and simulation were attributed to the improved STRs and weighting function (see Sections 3.2.7 and 3.2.8). (The calibration procedures for wire time offsets and drift chamber alignment were applied to the simulation, with the aim of degrading the resolution so that it matched the data better; however, these changes were found to be far less important than the STRs.)

The reconstruction resolution was measured in simulation using a special decay generator that emitted positrons according to a uniform angular distribution. A comparison of the true and reconstructed track parameters determined the momentum resolution within the kinematic fiducial: for the lower end of the spectrum at $p = 20 \text{ MeV}/c$, $\sigma(p)$ varied between $35 \text{ keV}/c$ and $110 \text{ keV}/c$, depending on the track's angle. For the upper end of the spectrum at $p = 50 \text{ MeV}/c$, $\sigma(p)$ varied between $70 \text{ keV}/c$ and $200 \text{ keV}/c$. The worst resolution (largest σ) corresponded to low angle tracks. The special simulation determined the average angle resolution as $\sigma(\cos \theta) = 0.002$ [17].

The distribution of energy loss through the target (Fig. 4.2(a)) is a Landau distribution that has been convoluted with a much wider Gaussian resolution function. The momentum dependence of this distribution's width can therefore be used to compare the reconstruction resolution in data and simulation. A full description of this technique is not included here since the implications for $P_\mu^\pi \xi$ are not significant; see Ref. [95] for further details.

Bibliography

- [1] S. Weinberg. A Model of Leptons. *Phys. Rev. Lett.*, 19(21):1264–1266, Nov 1967.
- [2] Donald Hill Perkins. *Introduction to High-Energy Physics; 4th ed.* Cambridge Univ. Press, Cambridge, 2000.
- [3] C. Amsler *et al.* Review of Particle Physics. *Phys. Lett. B*, 667(1-5):1–6, 2008. Review of Particle Physics.
- [4] D. Griffiths. *Introduction to Elementary Particles.* Wiley, 1987.
- [5] M. Goldhaber, L. Grodzins, and A. W. Sunyar. Helicity of Neutrinos. *Phys. Rev.*, 109:1015 – 1017, 1958.
- [6] D. Binosi and L. Theu β l. JaxoDraw: A graphical user interface for drawing Feynman diagrams. *Comput. Phys. Commun.*, 161:76–86, August 2004.
- [7] C.A. Gagliardi, R.E. Tribble and N.J. Williams. Global analysis of muon decay measurements. *Phys. Rev. D*, 72(7):073002, Oct 2005.
- [8] W. Fetscher, H.-J. Gerber and K.F. Johnson. Muon decay: complete determination of the interaction and comparison with the standard model. *Phys. Lett. B*, 173(1):102–106, 1986.
- [9] S. Eidelman *et al.* Review of Particle Physics. *Phys. Lett. B*, 592(1-4):1–5, 2004. Review of Particle Physics.
- [10] R.P. MacDonald *et al.* Precision measurement of the muon decay parameters ρ and δ . *Phys. Rev. D*, 78(3):032010, 2008.
- [11] A. B. Arbuzov. First-order radiative corrections to polarized muon decay spectrum. *Phys. Lett. B*, 524(1-2):99 – 106, 2002.
- [12] A. Czarnecki A. Arbuzov and A. Gaponenko. Muon decay spectrum: Leading logarithmic approximation. *Phys. Rev. D*, 65:113006, 2002.

-
- [13] A. Arbuzov and K. Melnikov. $\mathcal{O}(\alpha^2 \ln(m_\mu/m_e))$ corrections to electron energy spectrum in muon decay. *Phys. Rev. D*, 66:093003, 2002.
- [14] A. Arbuzov. Higher order QED corrections to muon decay spectrum. *J. High Energy Phys.*, 2003(03):063–063, 2003.
- [15] K. Melnikov C. Anastasiou and F. Petriello. The electron energy spectrum in muon decay through $\mathcal{O}(\alpha^2)$. *J. High Energy Phys.*, (09):014, 2007.
- [16] N. Danneberg *et al.* Muon Decay: Measurement of the Transverse Polarization of the Decay Positrons and its Implications for the Fermi Coupling Constant and Time Reversal Invariance. *Phys. Rev. Lett.*, 94:021802, 2005.
- [17] R.P. MacDonald. *A Precision Measurement of the Muon Decay Parameters ρ and δ* . PhD thesis, University of Alberta, 2008.
- [18] P. Herczeg. On muon decay in left-right-symmetric electroweak models. *Phys. Rev. D*, 34(11):3449–3456, Dec 1986.
- [19] V.M. Abazon *et al.* Search for W' Bosons Decaying to an Electron and a Neutrino with the D0 Detector. *Phys. Rev. Lett.*, 100:031804, 2008.
- [20] B. Jamieson *et al.* Measurement of $P_\mu \xi$ in polarized muon decay. *Phys. Rev. D*, 74(7):072007, 2006.
- [21] J.D. Jackson. *Classical Electrodynamics*. John Wiley & Sons, 1999.
- [22] V. Bargmann, L. Michel and V.L. Telegdi. Precession of the Polarization of Particles Moving in a Homogeneous Electromagnetic Field. *Phys. Rev. Lett.*, 2:435–436, 1959.
- [23] A. Balakin, V. Kurbanova and W. Zimdahl. Precession of a particle with anomalous magnetic moment in electromagnetic and gravitational pp-wave fields. *Gravity Cosmology Supplement*, 82:6–9, 2002.
- [24] P. Depommier. The BMT equation. Presentation to TWIST collaboration, May 2006.
- [25] P. Depommier. Muon depolarization in multiple scattering (TN100). Technical report, TWIST collaboration, TRIUMF, 2005.
- [26] W.H. Koppenol. Names for muonium and hydrogen atoms and their ions(IUPAC Recommendations 2001). *Pure Appl. Chem.*, 73:377–379, 2001.

- [27] M. Senba. Muon spin depolarization in noble gases during slowing down in a longitudinal magnetic field. *J. Phys. B: At. Mol. Opt. Phys.*, 31:5233–5260, 1998.
- [28] A. Jodidio *et al.* Search for right-handed currents in muon decay. *Phys. Rev. D*, 34(7), 1986.
- [29] A. Jodidio *et al.* Erratum: Search for right-handed currents in muon decay. *Phys. Rev. D*, 37(1), 1988.
- [30] J. H. Brewer. Muon spin rotation/relaxation/resonance. In *Encyclopedia of Applied Physics 11*, pages 23–53. 1994.
- [31] S.F.J. Cox. Implanted muon studies in condensed matter science. *J. Phys. C: Solid State Phys*, 20:3187–3319, 1987.
- [32] O. Hartmann *et al.* Diffusion of positive muons in some cubic metals. *Phys. Lett. A*, 61(2):141 – 142, 1977.
- [33] J. Brewer, University of British Columbia, Canada. Private communication.
- [34] W.B. Gauster *et al.* Measurement of the depolarization rate of positive muons in copper and aluminum. *Solid State Commun.*, 24(9):619–622, 1977.
- [35] W. Schilling. The physics of radiation damage in metals. *Hyperfine Interact.*, 4:636–644, 1978.
- [36] D.K. Brice. Lattice atom displacements produced near the end of implanted μ^+ tracks. *Phys. Lett. A*, 66:53–56, 1978.
- [37] P. Dalmas de Réotier and A. Yaouanc. Muon spin rotation and relaxation in magnetic materials. *J.Phys: Condens. Matter*, 9:9113–9166, 1997.
- [38] P. Dalmas de Réotier and A. Yaouanc. Quantum calculation of the muon depolarization function: effect of spin dynamics in nuclear dipole systems. *J.Phys: Condens. Matter*, 4:4533–4556, 1992.
- [39] A. Abragam. *Principles of Nuclear Magnetism*. International series of monographs on physics. Oxford University Press, 1986.
- [40] R.S. Hayano *et al.* Zero- and low-field spin relaxation studied by positive muons. *Phys. Rev. B*, 20:850, 1979.

- [41] W.J. Kossler *et al.* Diffusion and Trapping of Positive Muons in Al:Cu Alloys and in Deformed Al. *Phys. Rev. Lett.*, 41:1558–1561, 1978.
- [42] O. Hartmann *et al.* Coherent Propagation and Strain-Induced Localization of Muons in Al. *Phys. Rev. Lett.*, 41:1055–1058, 1978.
- [43] K.W. Kehr *et al.* Muon diffusion and trapping in aluminum and dilute aluminum alloys: Experiments and comparison with small-polaron theory. *Phys. Rev. B*, 26:567–589, 1982.
- [44] K.W. Kehr. Empirical information on quantum diffusion. *Hyperfine Interact.*, 17-19:63–74, 1984.
- [45] O. Hartmann. Diffusion and trapping of muons in aluminum: New experiments and comparison with Kondo theory. *Phys. Rev. B*, 37:4425–4440, 1988.
- [46] O. Hartmann. New results on diffusion in fcc metals. *Hyperfine Interact.*, 64:641–648, 1990.
- [47] O. Hartmann *et al.* Studies of μ^+ Localization in Cu, Al, and Al alloys in the Temperature Interval 0.03 – 100 K. *Phys. Rev. Lett.*, 44:337–340, 1980.
- [48] D.P. Stoker *et al.* Search for Right-Handed Currents by Means of Muon Spin Rotation. *Phys. Rev. Lett.*, 54:1887–1890, 1985.
- [49] D.P. Stoker, University of California, Irvine, USA. Private communication.
- [50] J. Korrynga. Nuclear magnetic relaxation and resonance (sic.) line shift in metals. *Physica*, 7-8:601–610, 1950.
- [51] S.J. Blundell and S.F.J. Cox. Longitudinal muon spin relaxation in metals and semimetals and the Korringa law. *J. Phys.: Condens. Matter*, 13:2163–2168, 2001.
- [52] J.H. Brewer *et al.* *Positive muons and muonium in matter*. Muon Physics. Academic Press Inc (London) Limited, 1975.
- [53] S.F.J. Cox *et al.* Muon Korringa relaxation. *Physica B*, 289-290:594–597, 2000.
- [54] R.H. Heffner. Muon spin depolarization in nonmagnetic metals doped with paramagnetic impurities. *Hyperfine Interact.*, 8:655–662, 1981.

- [55] J.A. Brown *et al.* Muon Depolarization by Paramagnetic Impurities in Nonmagnetic Metals. *Phys. Rev. Lett.*, 47:261–264, 1981.
- [56] B. Jamieson. *Measurement of the muon decay asymmetry parameter with the TWIST spectrometer*. PhD thesis, University of British Columbia, 2006.
- [57] T.D. Lee and C.N. Yang. Question of Parity Conservation in Weak Interactions. *Phys. Rev.*, 104(1):254–258, Oct 1956.
- [58] ARGUS collaboration. Determination of the Michel Parameters ρ , ξ , and δ in τ -Lepton Decays with $\tau \rightarrow \rho\nu$ Tags. *Phys. Lett. B*, 431:179–187, 1998.
- [59] L3 Collaboration. Measurement of the Michel parameters and the average tau-neutrino helicity from tau decays at LEP. *Phys. Lett. B*, 438:405–416, 1998.
- [60] R. Bartoldus. Measurements of the Michel Parameters in Leptonic Tau Decays using the OPAL Detector at LEP. *Nucl. Phys. B (Proc. Suppl.)*, 76:147–157, 1999.
- [61] R.L. Garwin, L.M. Lederman and M. Weinrich. Observations of the Failure of Conservation of Parity and Charge Conjugation in Meson Decays: the Magnetic Moment of the Free Muon. *Phys. Rev.*, 105:1415, January 1957.
- [62] G. R. Lynch, J. Orear, and S. Rosendorff. Muon decay in nuclear emulsion at 25 000 gauss. *Phys. Rev.*, 120(6):2277, Dec 1960.
- [63] M. Bardon, D. Berley, and L. M. Lederman. Asymmetry parameter in muon decay. *Phys. Rev. Lett.*, 2(2):56–57, Jan 1959.
- [64] Richard J. Plano. Momentum and asymmetry spectrum of μ -meson decay. *Phys. Rev.*, 119(4):1400–1408, Aug 1960.
- [65] Akhmanov *et al.* *Sov. J. Nucl. Phys*, 6:230, 1968.
- [66] I. Beltrami *et al.* Muon decay: Measurement of the integral asymmetry parameter. *Phys. Lett. B*, 194(2):326–330, 1987.
- [67] Ali-Zade *et al.* *Soviet Phys.-JETP*, 36 (9):940, 1959.
- [68] R.S. Hayano *et al.* Search for Right-Handed Currents in the Decay $K^+ \rightarrow \mu^+\nu$. *Phys. Rev. Lett.*, 52(5):329–332, Jan 1984.

- [69] J. Imazato *et al.* Search for right-handed currents in the decay chain $K^+ \rightarrow \mu^+\nu$, $\mu^+ \rightarrow e + \nu\bar{\nu}$. *Phys. Rev. Lett.*, 69(6):877–880, Aug 1992.
- [70] T. Yamanaka *et al.* Search for right-handed currents in the decay $K^+ \rightarrow \mu^+\nu$. *Phys. Rev. D*, 34(1):85–96, Jul 1986.
- [71] C.A. Coombes *et al.* Polarization of μ^+ Mesons from the Decay of K^+ Mesons. *Phys. Rev.*, 108(5):1348–1351, Dec 1957.
- [72] D. Cutts, T. Elioff, and R. Stiening. Muon Polarization and Energy Spectrum in $K^+ \rightarrow \pi^0 + \mu^+ + \nu$. *Phys. Rev.*, 138(4B):B969–B979, May 1965.
- [73] D. Cutts, R. Stiening, C. Wiegand, and M. Deutsch. Measurement of the Muon Polarization Vector in $K^+ \rightarrow \pi^0 + \mu^+ + \nu$. *Phys. Rev.*, 184(5):1380–1392, Aug 1969.
- [74] R.S. Henderson *et al.* Precision planar drift chambers and cradle for the TWIST muon decay spectrometer. *Nucl. Instrum. Methods Phys. Res., Sect. A*, 548:306–335, August 2005.
- [75] J. Hu *et al.* Time expansion chamber system for characterization of TWIST low-energy muon beams. *Nucl. Instrum. Methods Phys. Res., Sect. A*, 566:563–574, October 2006.
- [76] C.J. Oram, J.B. Warren and G.M. Marshall. Commissioning of a new low energy $\pi - \mu$ channel at TRIUMF. *Nucl. Instrum. Methods*, 179:95–103, January 1981.
- [77] J. Doornbos. The tuning of M13 for TWIST, theory and some results. Internal TWIST bulletin boards, December 2000.
- [78] R.E. Mischke, TRIUMF, Vancouver, Canada. Private communication.
- [79] T. Prokscha *et al.* The new μ E4 beam at PSI: A hybrid-type large acceptance channel for the generation of a high intensity surface-muon beam. *Nucl. Instrum. Methods Phys. Res., Sect. A*, 595.
- [80] J.E. Draper. Beam Steering with Quadrupole and with Rectangular Box Magnets. *Rev. Sci. Instrum.*, 37:1390, October 1966.
- [81] J. Musser. *Measurement of the Michel parameter ρ in muon decay*. PhD thesis, Texas A&M University, 2005.
- [82] Vector Fields. OPERA 3D simulation software. <http://vectorfields.com>.

- [83] G.M. Marshall, TRIUMF, Vancouver, Canada. Private communication.
- [84] A. Gaponenko. *A Precision Measurement of the Muon Decay Parameter δ* . PhD thesis, University of Alberta, 2005.
- [85] D. Wright. TN1: DME / He WC Gas Comparison. Technical report, TWIST collaboration, TRIUMF, October 1996.
- [86] LeCroy Corporation. 1877 Multihit Time-to-Digital Converter: Specification. <http://www.lecroy.com/lrs/dsheets/1877.htm>.
- [87] LeCroy Corporation. LeCroy 1877 Fastbus TDC Manual.
- [88] A. Hillairet. *Measurement of δ (in preparation)*. PhD thesis, University of Victoria, 2009.
- [89] R. Brun and F. Rademakers. ROOT - An Object Oriented Data Analysis Framework. *Nucl. Inst. & Meth. in Phys. Res. A*, 389:81–86, 1997.
- [90] R. Brun *et al.* GEANT, version 3.2114.
- [91] F. James. Fitting tracks in wire chambers using the Chebyshev norm instead of least squares. *Nucl. Instrum. Methods Phys. Res.*, 211(1):145 – 152, 1983.
- [92] R. Veenhof. Garfield - simulation of gaseous detectors. <http://garfield.web.cern.ch>.
- [93] C. Gagliardi, Texas A&M University, Texas, USA. Private communication.
- [94] P. Depommier. TN49: Muon polarisation in electromagnetic fields. Technical report, TWIST collaboration, TRIUMF, 2001.
- [95] R. Bayes. *Measurement of ρ (in preparation)*. PhD thesis, University of Victoria, 2009.
- [96] R. Bayes. Upstream stops discussion slides. Internal collaboration meeting presentation, January 2009.
- [97] G.R. Lynch and O.I. Dahl. Approximations to multiple Coulomb scattering. *Nucl. Instrum. Methods Phys. Res., Sect. B*, 58(1):6 – 10, 1991.
- [98] G. Marshall. OPERA map corrections from Hall and NMR maps at 2.0 T. Internal TWIST report, April 2009.

- [99] H. Yukawa. On the Interaction of Elementary Particles. *I, Proc. Phys.-Math. Soc. Jpn.*, 17:48, 1935.
- [100] C.D. Anderson and S.H. Neddermeyer. Cloud Chamber Observations of Cosmic Rays at 4300 Meters Elevation and Near Sea-Level. *Phys. Rev.*, 50:263–271, 1936.
- [101] S.H. Neddermeyer and C.D. Anderson. Cosmic-Ray Particles of Intermediate Mass. *Phys. Rev.*, 54:88–89, 1938.
- [102] S.H. Neddermeyer and C.D. Anderson. Nature of Cosmic-Ray Particles. *Rev. Mod. Phys.*, 11:191–207, 1939.
- [103] M. Riordan. *The Hunting of the Quark*. Sage Publications, 1987.
- [104] M. Conversi, E. Pancini and O. Piccioni. On the Disintegration of Negative Mesons. *Phys. Rev.*, 71:209–210, 1947.
- [105] E. Fermi, E. Teller and V. Weisskopf. The Decay of Negative Mesotrons in Matter. *Phys. Rev.*, 71:314–315, 1947.
- [106] C.M.G. Lattes, G.P.S. Occhialini and C.F. Powell. Observations on the Tracks of Slow Mesons in Photographic Emulsions Part 1. *Nature*, 160:453–456, 1947.
- [107] C.M.G. Lattes, G.P.S. Occhialini and C.F. Powell. Observations on the Tracks of Slow Mesons in Photographic Emulsions Part 1. *Nature*, 160:486–492, 1947.
- [108] T.D. Lee. A Brief History of the Muon. *Hyperfine Interact.*, 86:439–453, 1994.
- [109] C.S. Wu and V.W. Hughes. *Muon Physics: Introduction and History*. Academic Press Inc., 1977.
- [110] R.A. Millikan. Mesotron as the Name of the New Particle. *Phys. Rev.*, 1:105, December 1938.
- [111] C.D. Anderson and S.H. Neddermeyer. Mesotron (Intermediate Particle) as a Name for the New Particles of Intermediate Mass. *Nature*, 142:878, November 1938.
- [112] H. Lyle. Anderson, Carl. Interview by Harriett Lyle. Oral History Project, California Institute of Technology. Retrieved April 2008 from the World Wide Web: http://resolver.caltech.edu/CaltechOH:OH_Anderson_C, 1979.

- [113] A.H. Compton. Foreword: Symposium on Cosmic Rays. *Rev. Mod. Phys.*, 11:122, 1939.
- [114] H.J. Bhabha. The Fundamental Length Introduced by the Theory of the Mesotron (Meson). *Nature*, 143:276–277, February 1939.
- [115] J. L. Beveridge *et al.* A spin rotator for surface μ^+ beams on the new M20 muon channel at TRIUMF. *Nucl. Instrum. Methods Phys. Res., Sect. A*, 240:316–322, 1985.
- [116] Triumf CMMS. Helios superconducting solenoid. Website: <http://cmms.triumf.ca/equip/helios.html>.
- [117] G. Morris, TRIUMF, Vancouver, Canada. Private communication.
- [118] S.R. Dunsiger *et al.* Magnetic field dependence of muon spin relaxation in geometrically frustrated $\text{Gd}_2\text{Ti}_2\text{O}_7$. *Phys. Rev. B*, 73(172418), 2006.
- [119] F. James. MINUIT – Function Minimization and Error Analysis, CERN Program Library Entry D 506.
- [120] J.F. Ziegler. The stopping and range of ions in matter. <http://www.srim.org/>.
- [121] TRIUMF CS. TRIUMF Computing Services description of SRIM. <http://it-services.triumf.ca/scientific-computing/software/detector-engineering/srim-1>.
- [122] D.M. Garner. *Application of the muonium spin rotation technique to a study of the gas phase chemical kinetic of muonium reactions with the halogens and hydrogen halides.* PhD thesis, University of British Columbia, June 1979.
- [123] J. Doornbos, TRIUMF, Vancouver, Canada. Private communication.

Appendix I

$(g - 2)$ and the M13 beam line

The muons in the simulation are started at the end of the M13 beam line, with their spin and momentum anti-parallel. A small depolarisation takes place through the beam line, since there is a difference in the deflection of the momentum and spin through the magnetic fields of the dipoles. Recall from Eq. (1.37) that the precession frequencies for the momentum (ω_p) and spin (ω_s) differ by

$$\frac{\omega_p - \omega_s}{\omega_p} = a = \frac{g - 2}{2} = 1.17 \times 10^{-3}. \quad (\text{I.1})$$

For an on-axis particle, shown in Fig. I.1, the deviation from the initial momentum direction \vec{v}_0 will be equal in B1 and B2, but with opposite sign in each dipole. The same is true for the spin. Therefore the momentum and spin both have a net deflection of zero, and they remain anti-parallel.

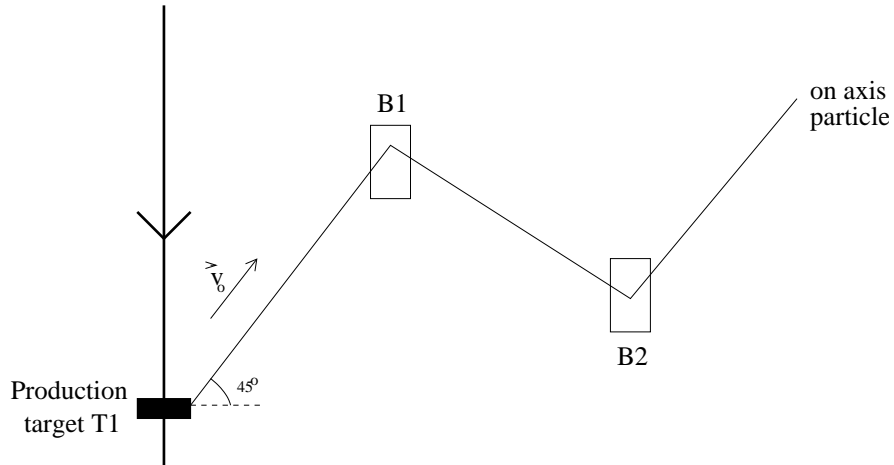


Figure I.1: An on-axis particle passing through M13.

Now consider the two most extreme trajectories that can pass through M13, assuming two different dipole configurations. These are shown in Fig. I.2. The real configuration is the single crossover in Fig. I.2(a)[123]. An upper limit can be set on the total net angular deflection using the emittance at the production target ($\lesssim 250$ mr, before focussing by Q1 and Q2) and TECs ($\lesssim 150$ mr). Under the configuration in Fig. I.2(a), the largest possible

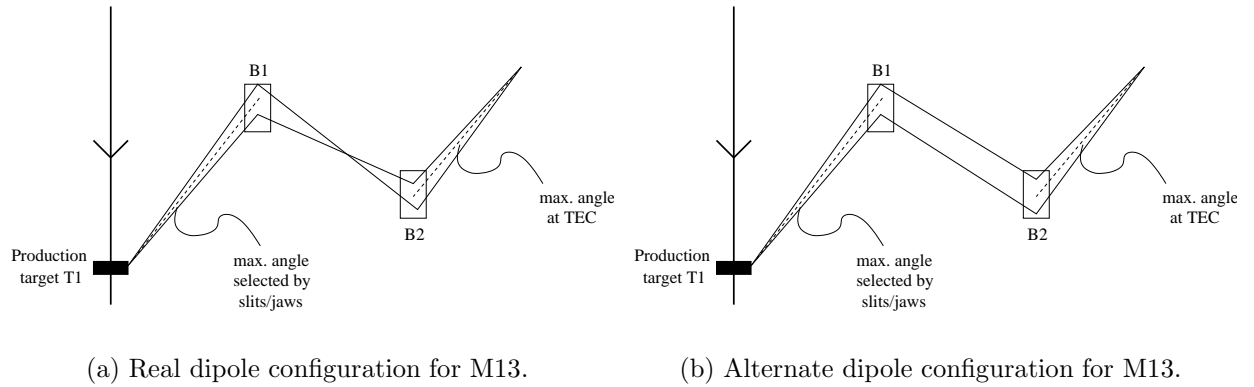


Figure I.2: Most extreme trajectories through M13 beam line, under two configurations.

deflection is ~ 100 mr, which from Eq. (I.1) changes the angle between the momentum and spin by $\Delta\theta \sim 1 \times 10^{-4}$. This contributes a depolarisation $\sim 1 - \cos \Delta\theta \sim 10^{-8}$. Even if the beam line were configured according to Fig. I.2(b), the depolarisation would be $\sim 10^{-7}$. Both of these depolarisation estimates are completely negligible.